Seyyed Hadi Seifi
Department of Industrial and Systems Engineering,
Mississippi State University,
Starkville, MS 39762
e-mail: ss4350@msstate.edu

Wenmeng Tian
Department of Industrial and Systems Engineering,
Mississippi State University,
Starkville, MS 39762
e-mail: tian@ise.msstate.edu

Haley Doude
Center for Advanced Vehicular Systems,
Mississippi State University,
Starkville, MS 39762
e-mail: haley@cavs.msstate.edu

Mark A. Tschopp
Fellow ASME
Army Research Laboratory,
Chicago, IL 60615
e-mail: mark.a.tschopp.civ@mail.mil

Linkan Bian[1]
Department of Industrial and Systems Engineering,
Center for Advanced Vehicular Systems,
Mississippi State University,
Starkville, MS 39762
e-mail: bian@ise.msstate.edu

Layer-Wise Modeling and Anomaly Detection for Laser-Based Additive Manufacturing

Additive manufacturing (AM) is a novel fabrication technique capable of producing highly complex parts. Nevertheless, a major challenge is the quality assurance of the AM fabricated parts. While there are several ways of approaching this problem, how to develop informative process signatures to detect part anomalies for quality control is still an open question. The objective of this study is to build a new layer-wise process signature model to characterize the thermal-defect relationship. Based on melt pool images, we propose novel layer-wise key process signatures, which are calculated using multilinear principal component analysis (MPCA) and are directly correlated with the layer-wise quality of the part. The resultant layer-wise quality features can be used to predict the overall defect distribution of a fabricated layer during the build. The proposed model is validated through a case study based on a direct laser deposition experiment, where the layer-wise quality of the part is predicted on the fly. The accuracy of prediction is calculated using three measures (i.e., recall, precision, and F-score), showing reasonable success of the proposed methodology in predicting layer-wise quality. The proposed quality prediction methodology enables online process correction to eliminate anomalies and to ultimately improve the quality of the fabricated parts. [DOI: 10.1115/1.4043898]

1 Introduction

Additive manufacturing (AM) techniques fabricate parts with complex shapes in a layer-by-layer manner, significantly reducing material waste and enabling new design options that are not feasible with conventional manufacturing technologies [1]. However, a major barrier that prevents broader industrial adoption of AM is that the quality of manufactured parts usually does not meet the stringent requirements of industrial application due to the existence of defects (e.g., porosity, cracks, and lack of fusion). There is an urgent need to develop layer-based quality measures for deposited layers so that correction actions can be taken to improve part quality during the fabrication [2,3]. Establishing an accurate process–defect relationship of the metal additive manufacturing through new layer-based process signatures can provide great value toward improving the part quality.

The challenges associated with the development of in situ layer-wise process signatures are twofold. First, there exists tremendous uncertainty in the underlying thermomechanical process of the metal printing associated with powder properties and process parameters. The existing finite element methods (FEMs) have been used to model the correlation between thermal history and microstructure properties. Temperature distribution and thermal behavior are the key properties for studying the thermomechanical process, affecting the residual stress, formation, and hardness as well as phase transformation during the AM process, which have been studied thoroughly by multiple research groups [4–7]. Moreover, the input parameters of an AM process influence the thermal history as well as mechanical properties significantly [8,9]. However, these FEM approaches are (1) dependent on part geometry, (2) time consuming, (3) nonrobust to process uncertainty (deterministic nature), and (4) computationally expensive.

Another group of methods uses advanced sensing technologies for in situ thermal monitoring. The resulting sensing data are high dimensional and have a low signal-to-noise ratio. Existing data-driven methods focus on statistical approaches to detect anomalies using observed thermal images [10–12]. Most of the existing works use local features for quality prediction purposes, and they cannot be directly utilized to characterize the profile of an entire deposited layer for multiple reasons, namely, (1) propagation of error, (2) negligence of between-layer variation, and (3) negligence of mushroom effect, which are discussed in detail in later sections. Hence, layer-wise modeling has attracted the attention of the AM community [2,3]. Layer-wise spatial porosity evolution has been modeled by Liu et al. based on X-ray computed tomography (XCT), which is a highly time consuming, expensive, and off-line characterization technique and, thus, very difficult to be used for in situ process monitoring [13].

In this work, we propose a data-driven methodology to extract thermal-based process signatures, which are directly correlated to the quality of the deposited layers. This represents a fundamental shift in the paradigm, from modeling and monitoring based on individual melt pools to layer-based modeling. To address the issue of high dimensionality of thermal history images, we propose to develop a tensor-based modeling approach to characterize the highly dynamic thermal–physical AM process captured by the pyrometer camera during the build. Figure 1(*a*) illustrates the initial structure and temporal trend of the captured images within the layer, and Fig. 1(*b*) demonstrates the tensor structures of the previously captured temporal data (see Secs. 3.1 and 3.2 for details). A central premise of the proposed methodology is that a consistent thermal history tends to lead to a homogenous microstructure of the deposited layers, resulting in more consistent part quality. To characterize the variability exhibited in the thermal history, multilinear

[1]Corresponding author.

Manuscript received August 4, 2018; final manuscript received May 23, 2019; published online June 21, 2019. Assoc. Editor: Qiang Huang.

This work is in part a work of the U.S. Government. ASME disclaims all interest in the U.S. Government's contributions.

Copyright © 2019 by ASME

Downloaded From: https://manufacturingscience.asmedigitalcollection.asme.org on 06/22/2019 Terms of Use: http://www.asme.org/about-asme/terms-of-use

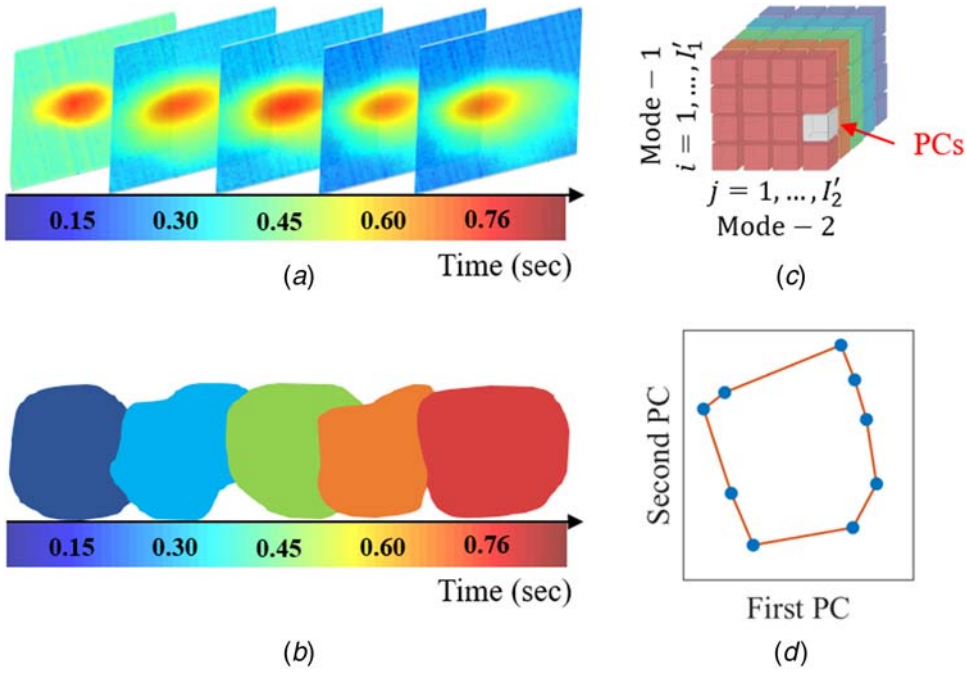

Fig. 1 Illustration of the four main steps toward achieving the key signatures: (*a*) initial layer-based thermal images, (*b*) tensor structure of the layer, (*c*) extracted principal components, and (*d*) layer-wise process signature

principal component analysis (MPCA) is utilized to extract the spatiotemporal variation pattern of thermal images as a tensor. Projecting the tensor data into a lower dimensional space leads to the core tensor shown in Fig. 1(*c*), in which critical information is condensed as principal components (PCs) (see Sec. 3.3 for details).

We propose a novel, layer-wise quality signature using the volume of convex hull formed by the multilinear principal components of all individual melt pools from the same layer fabrication. Figure 1(*d*) illustrates the geometric-based feature (convex hull) calculated by means of the PCs chosen from the low-dimensional tensor to predict the layer-wise quality (see Sec. 3.4 for details). We examine the uniqueness and sensitivity properties of the proposed layer-wise quality index and prove that it is a more suitable index (compared to symmetric shapes) to characterize the layer-wise melt pool consistency. The proposed methodology is validated using a real-world direct laser deposition (DLD) experiment. The predicted layer quality is compared to the outcome of the XCT characterization, which is regarded as the ground truth. This proposed new quality index provides the theoretical foundation for online process control/correction for the laser-based additive manufacturing process by accurately predicting the overall quality of deposited layers.

The remainder of the paper is organized as follows. Section 2 reviews the background studies in the literature; Sec. 3 provides the mathematical modeling of the proposed methodology; Sec. 4 discusses the case study used to validate the proposed methodology; Sec. 5 provides concluding remarks and the direction of possible future work; and Sec. 6 provides practical guidance for the practitioners for layer-wise quality prediction.

2 Literature Review

2.1 Defect Identification and Characterization of AM Parts. One major barrier in the broader industrial adoption of AM processes is their lack of robustness, stability, and repeatability caused by defects within the manufactured part, such as porosity, residual stress, minicracks, delamination, etc. [1]. According to Sharratt [14], causes of defects and anomalies can be grouped into three categories: (1) equipment-induced defects caused by improper performance, setting, and calibration of the main system components, (2) process-induced defects caused by process input parameters and previously melted materials, and (3) model-induced defects caused by choices implemented during the AM build design stage. All those sources directly influence the thermal distribution during the build, causing possible formation of defects within the AM parts. Therefore, the thermal history of AM processes contains critical information for AM part defect detection. Many researchers have studied the methods to identify part defects and deformations. For example, defects such as material cross-contamination (caused by the presence of foreign materials in powder), lack of fusion porosity, balling, and cracking have been investigated in laser powder bed fusion (LPBF) processes [15–18]. Moreover, part distortion and deformation is another major type of defect that has been extensively studied in different AM processes such as extrusion-based AM process, direct energy deposition, and fused filament fabrication [19–22]. In addition, process optimization helps minimizing the defects and thus improve the AM process output. Part build orientation, process parameters, and process condition optimization are thoroughly studied to minimize geometric deviations and improve AM fabrication quality [23–26].

Traditional defect characterization techniques have been used to pinpoint the defects within the AM parts. For example, postmanufacturing characterization techniques, such as XCT scanning and ultrasonic testing, have been extensively used to detect internal defects. Ultrasonic approaches have been primarily used to analyze the internal structure of parts in order to detect the defects such as pores, voids, cracks, and delamination [27,28]. For example, Cai et al. [29] proposed to use the nondestructive XCT technology to study the internal structure in order to characterize the relationship between process parameters and material porosity in a selective laser melting (SLM) process. They used an efficient image processing tool, which involved image enhancement and ring artifact removal before image segmentation. In another study, Liu et al. [13] proposed to model the spatial distribution of pores and their evolution inside a layer based on XCT scan data. This approach identifies the pore-prone areas in an AM part, which provides information on location and severity of the pores in different layers.

Although postmanufacturing characterization approaches provide valuable information on the internal structure of AM parts,

Downloaded From: https://manufacturingscience.asmedigitalcollection.asme.org on 06/22/2019 Terms of Use: http://www.asme.org/about-asme/terms-of-use

they are subject to the following limitations. Postmanufacturing characterization techniques, such as XCT scanning systems, are usually time consuming to implement. In addition, the accuracy of the ultrasonic approaches highly depends on the number of layers selected for inspection. Moreover, these approaches cannot serve for real-time modeling or monitoring for AM processes and, thus, cannot leverage the layer-by-layer nature of AM parts for in situ quality improvement purposes.

2.2 Process Modeling and Anomaly Detection. In this section, we focus on the literature pertaining to DLD and SLM processes, which are the two most common metal printing methods. DLD uses a powerful source of energy (i.e., a laser beam) to melt feedstock material (powder or wire) into a substrate to fabricate the design [30]. On the other hand, SLM consists of layers of powder spread on a platform, where powders in each layer are selectively fused together with a laser beam [31]. The main difference between DLD and SLM is that there is no powder bed in DLD processes, and the feedstock material is delivered simultaneously with the focused laser energy. For both DLD and SLM processes, the laser is the major energy source which dominates the part fabrication process. Thus, the thermal response as a function of time [32], i.e., the thermal history, is a salient process signature which carries important information about the microstructure of the as built part. Our method is based on the observed thermal history, and it can be potentially applied to both SLM and DLD processes.

Current studies on thermal history modeling and monitoring for AM processes can be categorized into two groups: finite element analysis methods and data-driven methods.

2.2.1 Finite Element Analysis Models. Many studies have been carried out using FEMs to model the thermal history. To name a few, Matsumoto et al. [4] proposed a method to simulate the fabrication process of a single layer using the SLM process. Kolossov et al. [5] modeled the temperature evolution and the formation of the sintered part using a three-dimensional FEM in a selective laser sintering process. A three-dimensional thermokinetic model was investigated by Crespo et al. [6], which is capable of simulating temperature field evolution and solid-state phase distribution during the laser powder deposition (LPD) of titanium. Martukanitz et al. [7] investigated a hybrid FEM (inactive/quiet element activation) to characterize the development and evolution of the microstructure during AM processes. Costa et al. [33] developed a three-dimensional thermokinetic FEM to simulate the changes of the phase transformation and properties during an LPD process. Costa et al. [34] developed a thermokinetic FEM for a multilayer LPD process. This model couples a finite element heat transfer model with a phase transformation kinetic data as well as a semi-empirical microstructure–property relationship model to finally calculate the hardness distribution of the part. Additionally, handful of recent studies has focused on thermal evolution modeling based on FEMs for thermal history prediction [35–44]. Defect prediction and thermal modeling can be done by macroscale and mesoscale FEMs. For example, porosity and lack of fusion defects have been investigated using finite element and numerical modeling [45–47]. Moreover, many studies have focused on thermal evolution and its effect on microstructural properties [48–50].

Although FEMs have been extensively used in modeling AM processes, they have some major limitations. First, the deterministic nature of FEM makes it difficult to take process uncertainty into account. Additionally, FEMs are usually computationally expensive, making them impractical for in situ quality control applications and unsuitable for industrial applications of quality/control. In addition, FEMs are highly dependent on part geometry, making them very difficult to be generalized to different geometries. Furthermore, model calibration and validation of FEMs requires additional data from real-world predictions. In summary, it is cumbersome to implement FEM approaches for real-time process monitoring/control and using data-driven methods relying on in situ sensing technology currently represents the most viable solution.

2.2.2 Data-Driven Approaches. The advanced sensing technologies have enabled in situ process monitoring based on thermal history collected using either pyrometers or infrared cameras. For data-driven approaches, the thermomechanical relationship is characterized using the statistical correlation between real-time sensing data and postprocessing microstructural properties. The thermal history of an AM fabrication is composed of a series of high-resolution thermal images which may be subject to low signal-to-noise ratio. Therefore, current data-driven approaches usually involve two steps: (1) dimension reduction (i.e., feature extraction) and (2) defect detection based on supervised or unsupervised learning algorithms.

In thermal images, melt pool represents the region of superheated molten metal in proximity to the laser–material interface, which contains critical information for process condition [32]. Melt pool morphological features, such as its depth, size, and temperature distribution, are used for process monitoring and anomaly detection [32,51]. For example, an anomaly detection approach was developed by Clijsters et al. [52] for the SLM process based on melt pool features captured by a co-axial pyrometer sensing system. Structural anomalies such as porosity can be directly linked to the process signatures extracted from the melt pool. A predictive control model was incorporated by Song and Mazumder [53] to control the melt pool temperature for a high-power diode laser cladding process. The authors used a double-color pyrometer camera for melt pool thermal monitoring. Subsequently, they proposed a state-space method to model the dynamics between the laser power and melt pool temperature for real-time closed-loop control. Moreover, Lane et al. [54] proposed to monitor the melt pool region using high speed thermographic measurements for a LPBF process. The area enclosed by the melt pool isotherms (contours) varies based on the location of the build stripes. Additionally, melt pool depth is directly correlated with deposited layer thickness, microstructure evolution, and pore formation. Having a high layer thickness may cause lack of fusion defects among consecutive layers or adjacent tracks which has been extensively studied [55–57].

Melt pool contours (i.e., the boundary of melting temperature of the fabricated material) have been recently investigated for anomaly detection in a DLD process [58,59]. Their proposed model does not depend on part geometry, and it can be easily generalized to different material properties as long as thermal history and defect information (for example, porosity) are available. Kanko et al. [60] proposed an in situ defect detection based on morphology measurements obtained from longitudinal sweeping of the imaging beam alongside the length of melt pool in an SLM process. Grasso et al. [10] proposed a model to detect and identify the anomalies in an SLM process by using a machine vision system in the visible range. They aimed to find the melt pools with different behaviors in terms of pixel intensity patterns over time. They used vectorized principal component analysis (PCA) to process the image data in order to apply a spatial version of Hotelling's T^2 statistics. Finally, a k-means clustering model is trained to detect and locate the anomalies during the layer-by-layer SLM process. In a subsequent study, the authors investigated statistical monitoring for different materials [11]. Krauss et al. [61] proposed a methodology to monitor the temperature distribution of a single layer alongside its evolution during the build using an off-axial thermography system. Their proposed methodology was able to detect anomalies such as process errors, pores, and other irregularities based on thermal distribution during an SLM process. Khanzadeh et al. [12] proposed a porosity prediction method based on the temperature distribution observed from the top of the melt pool. They used a self-organizing map method to analyze the melt pool images for anomaly detection.

The existing studies for porosity prediction use individual melt pools combined with clustering, classification, or control chart methods to detect anomalies [1,10,12,58]. Directly applying the existing methods to layer-wise quality prediction can lead to multiple drawbacks. If each melt pool has a potential misclassification probability of α, the misclassification probability of each layer

Downloaded From: https://manufacturingscience.asmedigitalcollection.asme.org on 06/22/2019 Terms of Use: http://www.asme.org/about-asme/terms-of-use

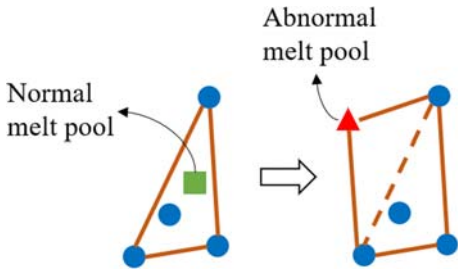

Fig. 2 Demonstration of the change in layer feature behavior due to a change in the single melt pool feature where square dot stands for a normal melt pool and triangle dot stands for an abnormal melt pool

with m melt pools is $1-(1-\alpha)^m$. If $\alpha = 0.01$, the misclassification probability of an arbitrary layer with 30 melt pools is 0.26 which is a very high error rate. This is similar with the idea of the multiple testing problem in statistical inference. Our method aims to resolve this issue while it extracts holistic features from layer-wise data for the quality prediction purposes.

The main contribution of the layer-wise study is quantifying the variability between multiple melt pools within a layer. By looking at the profile of the melt pools within the layer, we can obtain a holistic view about the variability. This means that our method can distinguish various types of defects (e.g., lack of fusion, entrapped gas, overheating, etc.) and capture different melt pool behaviors. As illustrated in Fig. 2, change in melt pool features leads to change in the convex hull boundary, which indicates a different thermal behavior.

In addition, layer-wise profiles can account for the shift in temperature distribution over layers due to the mushroom effect. The mushroom effect is a phenomenon that top layers tend to have wider shape compared to lower ones. This effect is a result of more hydrophilic melt pools due to bulk heating of the parts [32]. The shift in temperature results in improper comparison between melt pools of lower layers and upper layers. However, shift in temperature over layers changes the location of the convex hull, not the volume. Overall, volume of the convex hull is robust to the mushroom effect. Therefore, all the above-mentioned studies focus on process monitoring and anomaly detection based on individual thermal images, and thus, they are not capable of characterizing layer-wise process condition and part quality.

3 Methodology

3.1 Data Description and Challenges. The thermal history is usually captured as a discrete series of melt pool images by a pyrometer camera. When analyzing layer-wise thermal history, there are four major challenges: (1) high data dimensionality due to high sensor resolution, (2) corrupted images with no melt pool captured, (3) missing data in some pixels in the melt pool images (with unrealistic zero temperature), and (4) discrete image sampling, which leads to limited number of melt pool observations due to sensor sampling frequency. Examples of corrupted images and melt pool images with missing data are illustrated in Fig. 3. Moreover, due to the varying number of corrupted images within each layer, there is a significant variability in the number of melt pools observed within each layer. An example of an observed melt pool number distribution across all layers for a thin wall is illustrated in Fig. 4.

Conventional approaches analyze individual melt pool images and provide local porosity predictions [1,10,12,58]. Those approaches cannot deal with all the challenges concerning layer-wise modeling of thermal history. In the following sections, we propose a method to reduce the dimensionality of thermal images. Subsequently, layer-wise key process signatures are extracted through spatiotemporal variation within and between images. Finally, the classification model is built upon key process signatures for anomaly detection.

3.2 Data Transformation. Each melt pool is captured by the pyrometer camera as an image with a temperature reading at each pixel location within the field of view. Usually, the large size of these images (number of pixels) complicates processing without proper data reduction. Most importantly, the heat affected zone (HAZ) carries the main features of the melt pool and is usually condensed. Transforming the initial coordinate system and interpolating the temperature response surface can both emphasize the informative HAZ and reduce the data dimensionality (as shown in Fig. 5).

Converting the coordinate system from Cartesian to spherical enables melt pools with different sizes, shapes, and locations to have an identical support in the spherical domain [12]. Subsequently, incorporating a nonparametric surface interpolation (e.g., biharmonic model) allows the discrete data to be converted into a continuous form. With a continuous response surface, a relatively coarse grid of information can be extracted to effectively decrease the image size. Therefore, the overall data dimensionality decreases significantly. Considering the output of data transformation, each melt pool $\mathcal{M}_j$ is an image (second-order tensor) with size $I_1 \times I_2$.

3.3 Feature Extraction With MPCA. MPCA is a method developed to extract features of multidimensional data expressed as tensors [62]. One alternative approach is reshaping the melt pool images into large vectors (vectorization) and applying the traditional PCA method. However, vectorization causes computational and memory issues. Moreover, vectorization breaks the natural

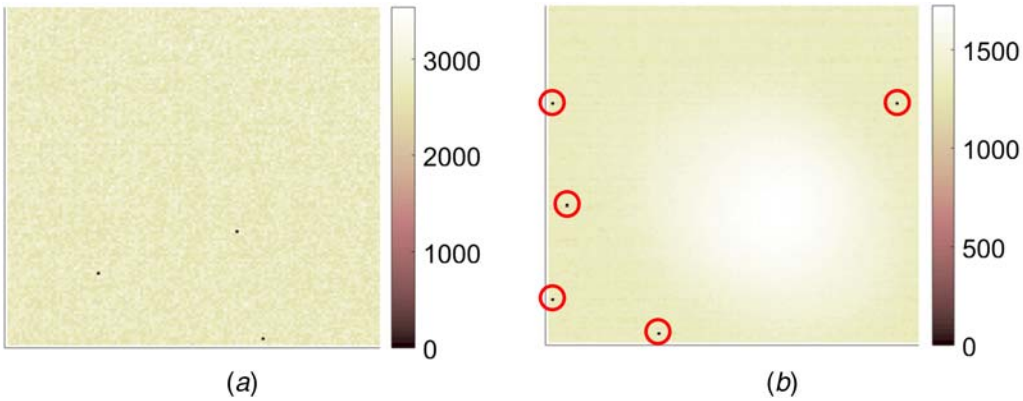

Fig. 3 Illustration of (*a*) corrupted image with no melt pool information and (*b*) melt pool with missing temperature measurements (circled)

Downloaded From: https://manufacturingscience.asmedigitalcollection.asme.org on 06/22/2019 Terms of Use: http://www.asme.org/about-asme/terms-of-use

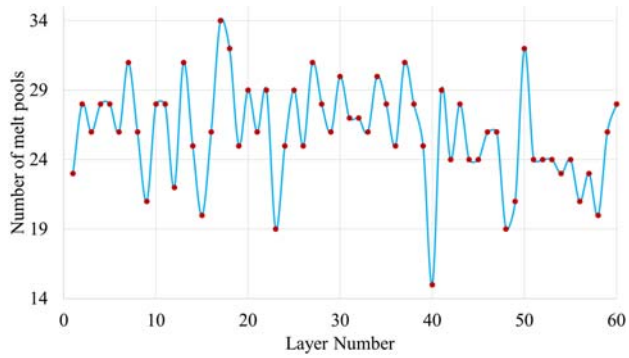

Fig. 4 An illustration of different number of melt pools within each layer when fabricating a 60-layer thin wall

correlation structure in the original melt pool images [62]. MPCA is a dimensionality reduction algorithm that works directly on tensor objects instead of vectors.

A set of N tensor objects $\{\mathcal{M}_1, \mathcal{M}_2, \ldots, \mathcal{M}_N\}$ is available for training. Each tensor object $\mathcal{M}_j \in \mathbb{R}^{I_1 \times I_2}$ accepts values from tensor space $\mathbb{R}^{I_1} \otimes \mathbb{R}^{I_2}$. The MPCA's goal is to perform a two-mode transformation to map the original tensor data into a low-dimensional tensor subspace. The two-dimensional melt pool data require two projection matrices $\{\tilde{U}^{(t)} \in \mathbb{R}^{I_t \times I'_t},\ t = 1, 2\}$ to map the melt pool images from the original tensor space $\mathbb{R}^{I_1} \otimes \mathbb{R}^{I_2}$ into a tensor subspace $\mathbb{R}^{I'_1} \otimes \mathbb{R}^{I'_2}$ where $I'_t < I_t$. The transformation equation is

$$\mathcal{M}'_j = \mathcal{M}_j \times_1 \tilde{U}^{(1)^T} \times_2 \tilde{U}^{(2)^T}, \quad j = 1, \ldots, N$$

where $\mathcal{M}'_j \in \mathbb{R}^{I'_1 \times I'_2}$ captures most of the variation in the original data. It is worth mentioning that the term PC mentioned in this MPCA-based study refers to the entries within the projected low-dimensional tensor $\mathcal{M}'_j$, which is not exactly the same concept as principal components extracted from traditional PCA.

To make sure the MPCA algorithm captures the major variability in the healthy melt pools, it is critical to train the model only based on the healthy melt pools to estimate the projection matrices. This is under the well accepted premise that the healthy melt pools share a similar thermal distribution.

3.4 Key Process Signatures of a Layer. It is desirable for a key process signature to carry the most informative features to discriminate healthy layers from unhealthy ones. In this section, two novel layer-wise key process signatures are proposed based on the low-dimensional subspace learned using the MPCA method.

3.4.1 Primary Feature: Volume of the Convex Hull. The first key process signature is derived from the PCs resulted from MPCA. This primary feature is proposed under the premise that the thermal history of a healthy layer has a smaller variability, and the main idea is to find a measure to capture the dispersion of the PCs of all melt pools within one layer. Being unhealthy

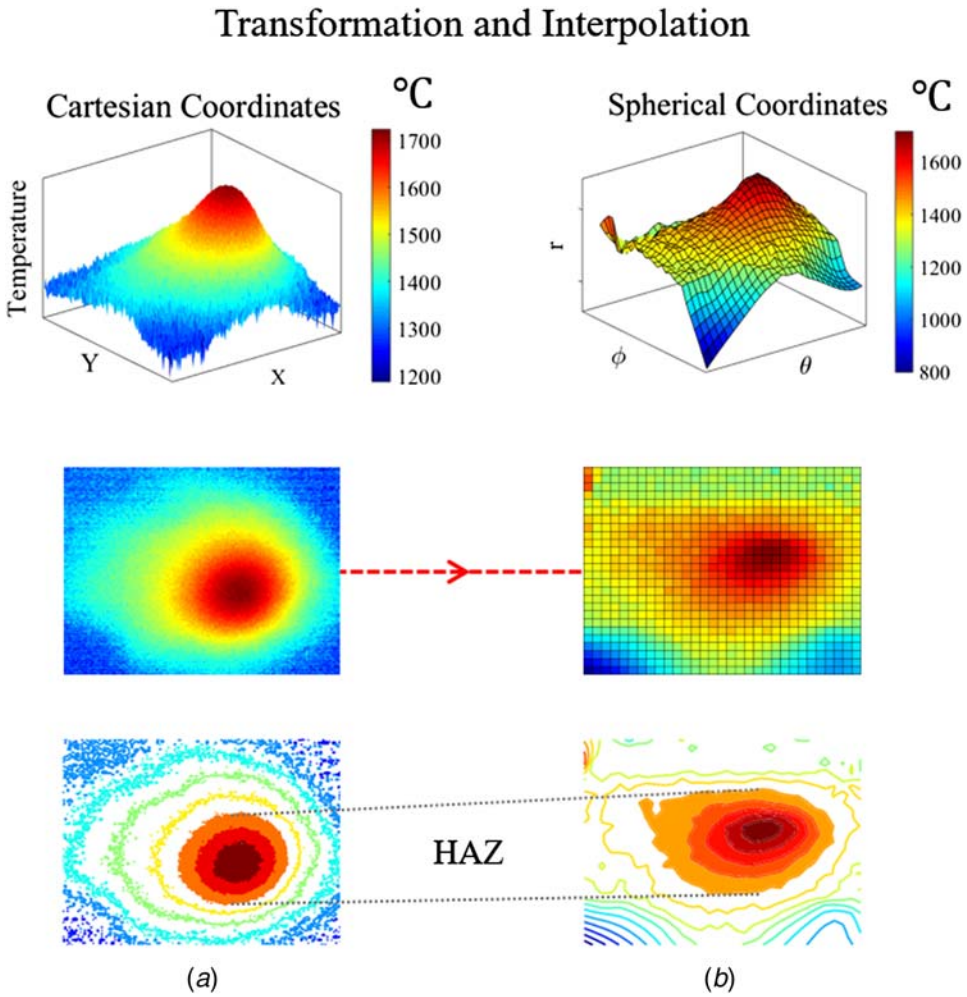

Fig. 5 Illustration of data transformation where (*a*) is the initial high dimensional data and (*b*) is the low-dimensional extracted grid with emphasis on heat affected zone

Downloaded From: https://manufacturingscience.asmedigitalcollection.asme.org on 06/22/2019 Terms of Use: http://www.asme.org/about-asme/terms-of-use

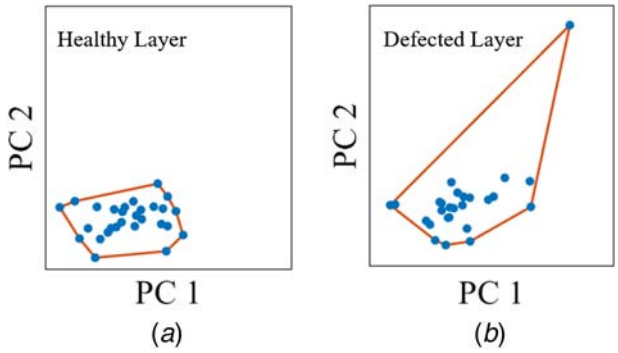

Fig. 6 Illustration of the primary layer-wise key signature. Examples of (*a*) a healthy layer and (*b*) an unhealthy layer based on the first two PCs extracted from MPCA.

causes at least one melt pool to have a major difference in PCs compared to the healthy ones which leads to a more scattered distribution (as shown in Fig. 6).

To capture the dispersion, one reasonable approach is building a convex hull using the PCs of all the melt pools observed in one layer. Although, other geometries, such as minimal bounding sphere, can also be utilized to enclose the points and characterize the dispersion, convex hull builds a unique free form shape enclosing all data points, and it is also highly sensitive to the outliers in the enclosed data points. Two theorems below demonstrate the advantages of using the convex hull over the minimal bounding sphere. Before proving the theorems, formal definitions of the convex hull and the minimal bounding sphere are provided.

DEFINITION 1. *Convex hull: The convex hull of a finite point set C is the intersection of all convex supersets containing C. Given that C contains n points $c_1, c_2, \ldots, c_n$, the convex set of C is represented as* $conv(C) = \left\{\sum_{i=1}^{n} \lambda_i c_i | c_i \in C,\ \lambda_i \geq 0,\ \sum_{i=1}^{n} \lambda_i = 1\right\}$ [63].

DEFINITION 2 (Minimal bounding sphere). *The smallest bounding sphere $\omega(C)$ is the hypersphere with the smallest radius which encloses a given point set C in its interior or on its boundary; i.e.,* $\|c_i - O\| \leq R \forall\, i \in 1, \ldots, n$, *where O and R represent the center and the radius of* $\omega(C)$, *respectively.*

THEOREM 1 (Sensitivity). *Adding a new point x^* to set C such that $x^* \notin conv(C)$, the convex hull will definitely get enlarged. On the other hand, its smallest bounding sphere may not always change.*

Proof. If $\exists \lambda_i^* : x^* = \sum_{i=1}^{n} \lambda_i^* c_i,\ \lambda_i^* \geq 0,\ \sum_{i=1}^{n} \lambda_i^* = 1$, then $x^* \in conv(C)$ and $conv(C \cup \{x^*\}) = conv(C)$. Additionally, for the bounding sphere, $\|x^* - O\| = \left\|\sum_{i=1}^{n} \lambda_i^* (c_i - O)\right\| \leq \sum_{i=1}^{n} \lambda_i^* \|c_i - O\| \leq \sum_{i=1}^{n} \lambda_i^* R = R$, thus $\omega(C \cup \{x^*\}) = \omega(C)$. If $\nexists \lambda_i^* : x^* = \sum_{i=1}^{n} \lambda_i^* c_i,\ \lambda_i^* \geq 0$, and $\sum_{i=1}^{n} \lambda_i^* = 1$, we need to add x^* to the basis of the convex combinations which updates the supersets and extends the convex hull to $conv(C \cup \{x^*\}) = \{\sum_{i=1}^{n} \lambda_i c_i + \lambda_{n+1} x^* | c_i \in C,\ \lambda_i \geq 0,\ \sum_{i=1}^{n+1} \lambda_i = 1\} \supset conv(C)$. Moreover, regarding the bounding sphere, $\exists x^*$ such that $x^* \notin conv(C)$ and $\|x^* - O\| \leq R$, $\omega(C \cup \{x^*\}) = \omega(C)$; and if $\|x^* - O\| > R$, the radius R needs to be enlarged to enclose x^*, i.e., $\omega(C \cup \{x^*\}) \supset \omega(C)$. ■

THEOREM 2 (Conditional uniqueness). *Each point set has its own unique convex hull provided a fixed set of extreme points.*

Proof. Suppose we have one set of n points C. Assume that two different points $x_1^* \neq x_2^*$ are added separately to set C where

$$\nexists \lambda_i^* : x_1^* = \sum_{i=1}^{n} \lambda_i^* c_i,\ \lambda_i^* \geq 0, \text{ and } \sum_{i=1}^{n} \lambda_i^* = 1$$

$$\nexists \lambda_i^* : x_2^* = \sum_{i=1}^{n} \lambda_i^* c_i,\ \lambda_i^* \geq 0, \text{ and } \sum_{i=1}^{n} \lambda_i^* = 1$$

which means both points are extreme points, and according to Theorem 1, adding either of them to set C will enlarge the convex hull into a new one where $conv(C \cup \{x_1^*\}) \neq conv(C \cup \{x_2^*\})$. On the other hand, if $\|x_1^* - O\| \leq R$ and $\|x_2^* - O\| \leq R$, the boundary sphere stays the same even though new extreme points have been added to the set, i.e., $\omega(C \cup \{x_1^*\}) = \omega(C \cup \{x_2^*\}) = \omega(C)$. In summary, while convex hulls of two different sets are different, their corresponding minimal boundary spheres can be identical. ■

Volume of the convex hull measures the dispersion of the points in the high dimensional space. The more dispersion within data points, the larger volume of the convex hull. The algorithm on how to calculate the volume of a high dimensional convex hull is provided in Ref. [64].

3.4.2 Secondary Feature: Maximum Norm of Residuals. Although the convex hull is an effective measure for layer-wise thermal characteristics, the extracted PCs may not capture all the variation in the original data. Additionally, a valuable portion of information may get lost during projection from a higher dimensional tensor to a lower dimensional one. This is the reason why another signature feature should be introduced to account for the part not considered in the primary feature.

Each melt pool after projection loses a portion of data, whose amount differs from one melt pool to another. Backward projection of each melt pool using the projection matrices $\tilde{U}^{(t)}$ will create a tensor with the same dimension as the original tensor. Subtracting these two tensors generates the residual tensor. Backward projection is performed as follows:

$$\mathcal{M}_j'' = \mathcal{M}_j' \times_1 \tilde{U}^{(1)} \times_2 \tilde{U}^{(2)}, \quad j = 1, \ldots, N$$

where $\mathcal{M}_j''$ accepts value from tensor space $\mathbb{R}^{I_1} \otimes \mathbb{R}^{I_2}$, same as its initial tensor $\mathcal{M}_j$. Therefore, the residual tensor is $\mathcal{R} = \mathcal{M}_j - \mathcal{M}_j''$. One way to represent this residual tensor is through the L^1 norm. Since the MPCA model is trained based on healthy melt pools, it is expected that projecting unhealthy melt pools results in either significantly different PC values or significantly larger residuals compared to the healthy ones. Choosing the maximum norm of residuals inside a layer is one effective way of capturing anomalies. If there exists at least one unhealthy melt pool inside a layer, it causes the maximum norm of residuals to increase remarkably (as shown in Fig. 7). This is similar to the idea of group control chart in statistical quality control [65].

3.5 Classification: Correlating Layer Signatures to Structural Quality. After defining the signature features (i.e., the convex hull volume and the norm of residuals), the classification model can be trained. The goal of the classifier is to draw a boundary between healthy layers and unhealthy layers, which can be used to predict the labels of newly observed layers. As mentioned before, if one layer contains at least one porosity, it is labeled as unhealthy (as shown in Fig. 8). The classifier's input includes one vector of response labels (0 if healthy, 1 if unhealthy) and a matrix of two predictors: the convex hull volume and the maximum norm of residuals.

Numerous supervised learning algorithms can be applied to the extracted features for layer-wise quality prediction. In this paper, support vector machine (SVM) is selected as it is one of the most powerful supervised machine learning techniques [66]. Detailed discussion on SVM can be found in [67].

The objective of SVM methods is to find a hyperplane so that the distance from the hyperplane to the nearest data point on each side is maximized. In many real-world problems, instances of different classes are not linearly separable. One solution is mapping data into higher dimensional space where we can define a new separating hyperplane. Kernel functions are a class of special functions which make this mapping possible through defining inner products directly in the feature space.

In this study, the Gaussian class of kernels is selected due to the high flexibility this type of kernel functions can provide comparing to their linear counterparts. Using Gaussian kernels

Downloaded From: https://manufacturingscience.asmedigitalcollection.asme.org on 06/22/2019 Terms of Use: http://www.asme.org/about-asme/terms-of-use

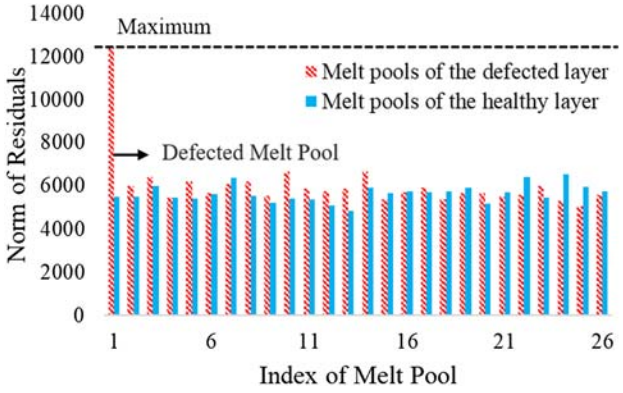

Fig. 7 Demonstration of the norm of residuals for melt pools of two layers. Patterned bars are the norms for melt pools of the unhealthy layer where solid bars are for the healthy layer. There is only one defected melt pool in the defected layer which demonstrates the maximum norm of residuals.

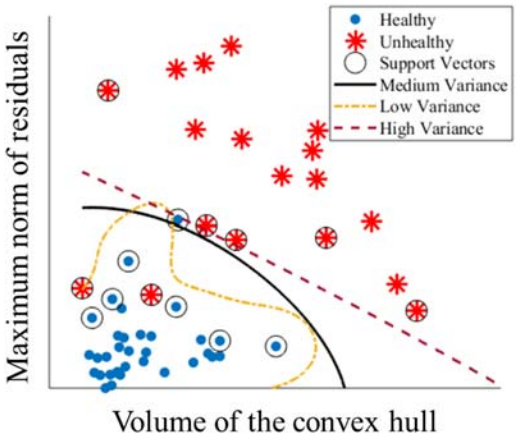

Fig. 9 Comparison of three different kernel variations of Gaussian family

requires selection of the scale parameter (variance). In general, a lower variance provides more flexibility when used in SVM classification.

If there are p predictors, low-variance Gaussian kernel function (variance $= (\sqrt{p}/4)$) makes finely detailed distinctions between classes (at the cost of overfitting in some cases); medium-variance Gaussian kernel function (variance $= (\sqrt{p})$) has lower flexibility than low-variance Gaussian and prevents overfitting issue; high-variance Gaussian kernel function (variance $= (4 \times \sqrt{p})$) makes coarse distinction between the data classes. Medium-variance Gaussian is the suitable choice of classification in this study where low-variance Gaussian has the risk of overfitting and the high-variance Gaussian has the risk of low capacity, as illustrated in Fig. 9.

3.6 Hyperparameter Tuning. The number of PCs chosen to form a convex hull for each layer affects the output of prediction. The number of PCs is regarded as a hyperparameter of the model and the best way to determine its value is cross validation.

At each testing iteration (Secs. 4.4 and 4.5), all the layers are divided into two mutually exclusive subsets, training and testing sets. Within training set, a k-fold cross validation is performed, and the performance of the model is evaluated using different numbers of PCs (dimension of convex hull). This procedure is illustrated in Fig. 10. The value of k depends on the size of the training set which is determined in both of the following sections. In case of multiple dimensions (number of PCs) with maximum F-score, the median of the set is selected.

The performance of the classification model can be evaluated using three measures, namely, precision, recall, and F-score. Those measures can be calculated using the formulas as follows:

$$\text{Recall} = \frac{\text{True positive}}{\text{True positive} + \text{false negative}}$$

$$\text{Precision} = \frac{\text{True positive}}{\text{True positive} + \text{false positive}}$$

where true and false terms refer to correct and incorrect predictions, respectively. Positive and negative terms refer to the predicted classes of unhealthy and healthy layers. For example, true positive is defined as the number of unhealthy layers that are accurately classified as unhealthy. F-score is the harmonic mean of precision and recall.

$$\text{F} - \text{score} = 2 \times \frac{\text{precision} \times \text{recall}}{\text{precision} + \text{recall}}$$

4 Case Study

The performance of the proposed methodology is examined using a direct laser deposition process which fabricates a thin wall using Ti-6AL-4V. During the build of this thin wall, a pyrometer camera captures the thermal images of melt pools at different locations of the thin wall. After the fabrication, XCT scans are used to characterize the layer-wise porosity structure inside the build.

4.1 Experimental Setup. The experimental setup consists of a LENS 750 machine equipped with thermal imaging camera, one co-axial pyrometer camera to capture melt pools (Stratonics, Inc.), and one infrared camera to capture the global heat flow

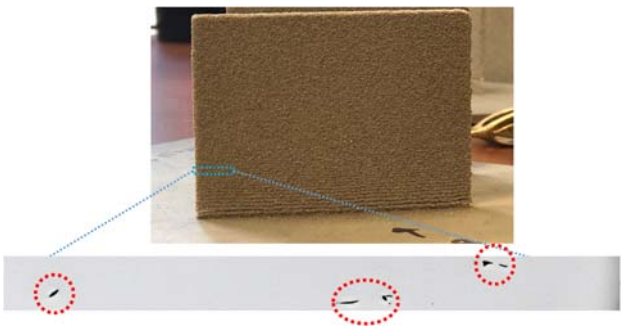

Fig. 8 The illustration of the part of an unhealthy layer which includes pores

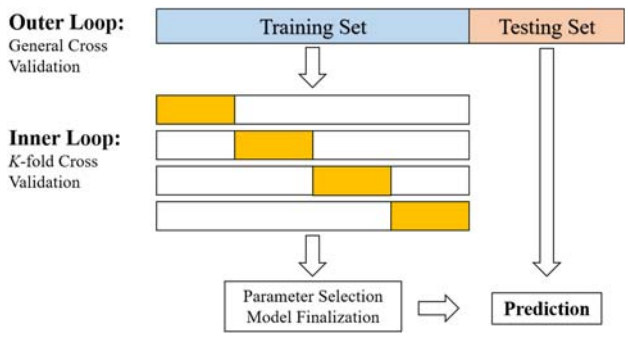

Fig. 10 General overview of parameter selection using cross validation

Downloaded From: https://manufacturingscience.asmedigitalcollection.asme.org on 06/22/2019 Terms of Use: http://www.asme.org/about-asme/terms-of-use

(Sierra-Olympic Technologies, Inc. Viento320). The pyrometer camera mentioned in this study is referring to the melt pool sensor which provides precise temperature measurements by means of two-wavelength (λ) pyrometry technology.[1]

In this study, melt pool images captured by the pyrometer camera are used to build the prediction model. The pyrometer camera characteristics are as follows:

- Exposure time: 2.0274 ms (reduces the risk of motion blur)
- CMOS detector with array size 752×480 and pixel pitch 6.45 μm
- Captured temperature range: 1000–2500 °C
- Pixel clock: 5 MHz
- Nominal image collection rate: 6.4 Hz

The powder used is titanium alloy Ti-6AL-4V. Table 1 summarizes the initial process parameters used to fabricate the thin walls with height 27.56 mm, length 47.81 mm, and thickness 1.78 mm [68].

After the fabrication, the parts are scanned with a high-resolution (1 μm precision) XCT scan machine to detect anomalies. For a high-quality scan, Al + Cu filter is used to block out low-energy rays. Part is rotated inside the chamber (0.5 deg in each step), and in each step it is exposed to X-ray beams for 1400 ms to capture the image. More information about the XCT scanning process can be found in [69].

4.2 Dataset Description. The thin wall includes 60 layers where each layer contains several melt pools in a temporal order. Based on the XCT results, 26 layers include at least one pore. These 60 layers of data are divided into two sets, the first part of data is used to train the model and second part is used to test the performance of the proposed method. Before dividing data into training and testing sets, all thermal images with size 752×480 are cropped to images with size 130×130, the universal region which carries the important information about the melt pool. Afterwards, these images are transformed into spherical coordinates and interpolated with a biharmonic model. The interpolation model is used to extract a lower dimensional grid of data, and thus, each image with size 130×130 is transformed into a new grid with size 27×32. After data transformation, MPCA is applied for dimension reduction, and key signature features are extracted based on the extracted PCs.

4.3 Benchmark Method. In this section, a traditional scheme is demonstrated which combines Hotelling's T^2 statistics and their variability within one layer to detect unhealthy layers. It is worth mentioning that the numbers of melt pools differ among different layers, and therefore, traditional statistics (like Hotelling's T^2) cannot be directly applied to the layer-wise data. Some additional steps need to be taken to account for the different numbers of melt pools within different layers. One way is to calculate a single Hotelling's T^2 statistic based on each individual melt pool and then use a traditional quantification, the variance of all the T^2 statistics observed from one layer, to characterize the layer-wise dispersion.

After applying the MPCA algorithm for dimension reduction, Hotelling's T^2 statistics can be calculated for each individual melt pool using the equation as follows:

$$\chi_0^2 = (x-\mu)'\Sigma^{-1}(x-\mu)$$

where x is a $p \times 1$ vector of the extracted PCs, μ is the mean vector of PCs, and Σ is its covariance matrix. With the statistics of each melt pool, the variability within each layer is calculated. It is expected that the layers with higher variance contain at least one porosity.

Similar to the proposed methodology, the mean μ and covariance matrix Σ of the extracted PCs are estimated using the training set.

[1]http://stratonics.com/systems/sensors/

Table 1 Illustration of process parameters used for the fabrication of thin wall

Laser power	290 W	Scan speed	12.70 mm/s
Powder feed rate	0.32 g/s	Hatch spacing	0.508 mm
Substrate thickness	3.3 mm	Starting offset from substrate	6.7 mm
Layer thickness	0.508 mm	Nozzle diameter	1.016 mm

The variance feature extracted from Hotelling's T^2 replaces the convex hull-based feature to quantify the dispersion within each layer, and the classifier is trained based on the maximum norm of residuals and the variance of the T^2 statistics within one layer.

For a fair comparison, the same cross-validation procedure is applied for both the proposed methodology and the benchmark method. The selection procedure of the number of PCs are identical for both methods with one exception, where Hotelling's T^2 can use all the available PCs to train the covariance matrix.

4.4 Leave-One-Out Cross Validation. Leave-one-out is an N-fold cross validation where N represents the number of samples. Training set consists of $N-1$ layers where a six-fold cross validation is used to determine the number of PCs. The confusion matrix after applying both models to the 60 layers is shown in Table 2. Additionally, the histogram shown in Fig. 11 demonstrates the frequency of the number of PCs used in the proposed and benchmark methods within all steps of leave-one-out cross validation.

Comparing the results shown in Table 2, the proposed methodology has significantly better performance especially for predicting the unhealthy layers. The benchmark method has lower accuracy in terms of all the quality measures.

As is shown in Table 2, there are two unhealthy layers that are misclassified as healthy (i.e., two false negatives) and one healthy layer (i.e., one false positive) that is classified as unhealthy. Those false negatives, though identified as unhealthy from XCT scans, demonstrate normal thermal behavior based on the observed thermal history. This may be due to the missing melt pool images within those layers because of either the limited sampling rate or the corrupted image data. The false positive behaves as unhealthy which may be due to corrupted images collected by the thermal camera during the fabrication process.

4.5 Monte-Carlo Cross Validation. Repeated random subsampling validation, also known as Monte-Carlo cross validation, randomly splits dataset into training and testing sets [70]. Training and testing sets are randomly assigned with 50 and 10 layers, respectively. Within the training set, a six-fold cross validation is performed to determine the number of PCs leading to a better classification performance. Finally, the performance of both models is tested based on the testing set.

This random selection is performed 500 times and all the three measures are calculated for each iteration. In each iteration, misclassified layers, if any, are removed from training set until all the layers are classified correctly. The histogram of the number of PCs chosen in each iteration is shown in Fig. 12. The mean and standard deviation (SD) values for the recall, precision, and F-score for both methods are shown in Table 3.

According to Table 3, proposed methodology significantly outperforms the benchmark method with respect to all the quality measures. Therefore, the convex hull-based approach defines a more reliable quality feature concerning the anomalies detection within layers compared to the Hotelling's T^2 approach.

The output of one iteration of the proposed methodology is illustrated in Fig. 13 as an example where there are five healthy and five unhealthy layers in the testing set. Nine out of ten layers are classified correctly and only one unhealthy layer is misclassified as healthy. The classification model uses the medium-variance

Downloaded From: https://manufacturingscience.asmedigitalcollection.asme.org on 06/22/2019 Terms of Use: http://www.asme.org/about-asme/terms-of-use

Table 2 Confusion matrix for the leave-one-out cross validation

		Proposed method				Benchmark method		
		Predicted				Predicted	
		Healthy	Unhealthy			Healthy	Unhealthy
Actual	Healthy	33 (97%)	1 (3%)	Actual	Healthy	33 (97%)	1 (3%)
	Unhealthy	2 (8%)	24 (92%)		Unhealthy	5 (19%)	21 (81%)
Classification Accuracy							
Recall		Precision	F-Score		Recall	Precision	F-Score
0.92		0.96	0.94		0.81	0.95	0.87

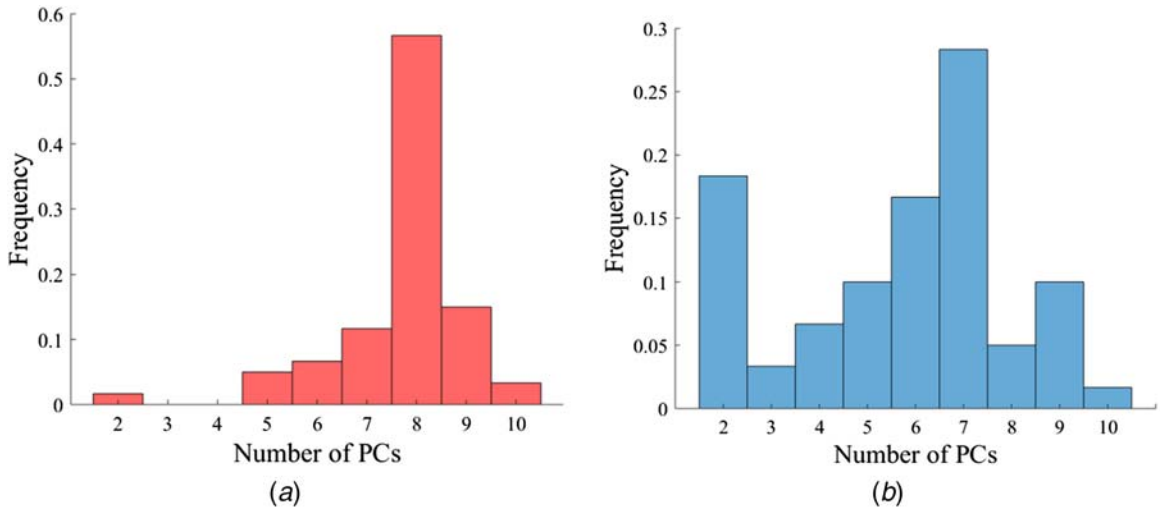

Fig. 11 Illustration of the frequency of selected number of PCs in leave-one-out cross validation: (*a*) proposed and (*b*) benchmark methodology

Gaussian kernel function to classify the layers, which is shown with black line in Fig. 13. The bottom-left region of the line is classified as healthy.

5 Conclusion

The main challenge in the additive manufacturing process is its lack of repeatability, leading to quality issues such as internal porosity, minicracks, and lack of fusion in the build. These issues are the main barrier for broader industrial adoption of AM technologies in the demanding industries. A wide variety of approaches in the literature are focused on characterizing the defects by modeling the thermomechanical relationship, i.e., FEMs, which suffer from limitations such as low computational efficiency, high geometric dependence, and nonrobustness to process uncertainty. Data-driven approaches can address these limitations by characterizing the defects based on features extracted from observed thermal history. However, existing data-driven

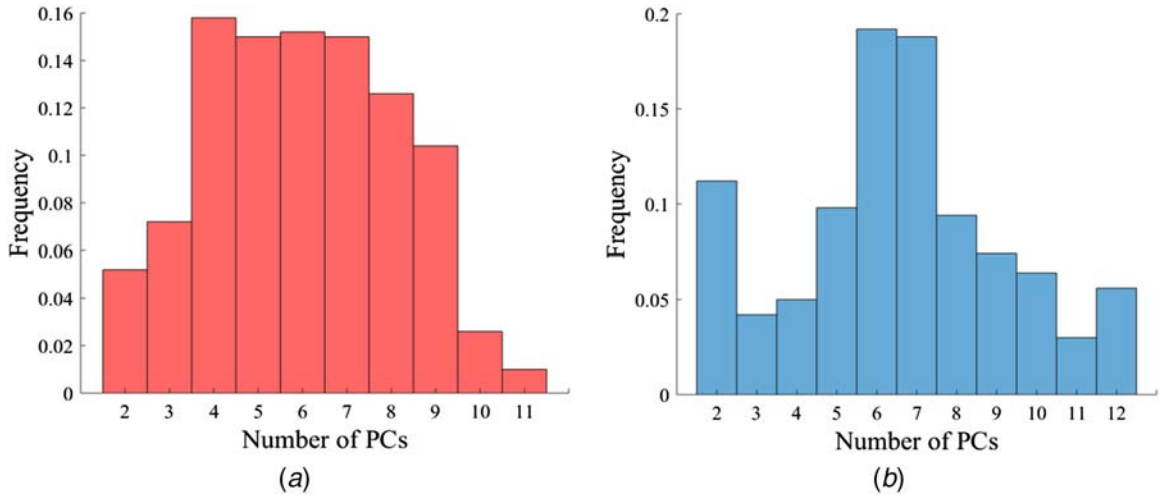

Fig. 12 Illustration of the frequency of selected number of PCs in Monte-Carlo cross validation: (*a*) proposed and (*b*) benchmark methodology

Downloaded From: https://manufacturingscience.asmedigitalcollection.asme.org on 06/22/2019 Terms of Use: http://www.asme.org/about-asme/terms-of-use

Table 3 Summary of mean quality measures with their SD in parentheses

	Recall	Precision	F-score
Proposed	0.8930 (0.1525)	0.9617 (0.0930)	0.9165 (0.1083)
Benchmark	0.8495 (0.1711)	0.9285 (0.1441)	0.8750 (0.1257)

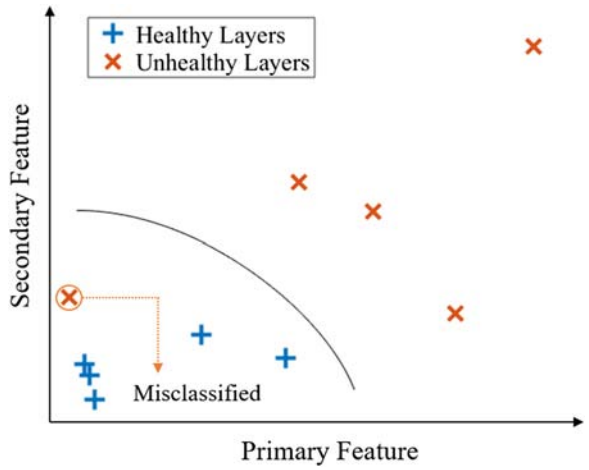

Fig. 13 Illustration of one iteration of Monte-Carlo cross validation

methods provide porosity prediction based on individual melt pool images only, which cannot be directly used for layer-wise quality prediction and process control.

In this paper, a novel online layer-wise quality prediction methodology is proposed. First, the data-driven transformation techniques are used to reduce the dimension of images, which brings the images into an identical support and focuses on HAZ; subsequently, two novel layer-wise process signatures are derived based on the tensor decomposition of melt pool images of the entire layer using MPCA. The SVM classifier is used for real-time layer-wise quality prediction based on the proposed key signatures. The performance of the proposed methodology is validated through two cross-validation techniques and is compared with a benchmark method which combines traditional statistical approaches. The proposed method can serve as a solid foundation for in situ process control/correction actions for AM quality improvement.

A couple of interesting topics still remain open for future research. First, the proposed method does not account for the possible interactions between adjacent layers/tracks. One of the important between-layer interactions is the remelting effect which refers to a phenomenon where the heat generated when depositing a new layer may remelt the recently deposited layers/tracks and potentially correct the porosity formed in previous layers. Second, the performance of the proposed method needs further investigation when it is applied to complicated geometry fabrication. Last but not the least, layer-wise process control algorithms are needed to work together with the monitoring scheme to adjust the process parameters for quality improvement.

6 Note to Practitioners

In this section, a step-by-step procedure is summarized to guide the practitioners on how the proposed methodology can be used for in situ layer-wise quality prediction. All the computations in this paper are implemented using MATLAB, and all the codes are available upon request. The experimental setup needed includes a co-axial dual wavelength pyrometer camera for in situ data collection and an XCT system for off-line validation. Prior to the data collection, the sensor systems need to be properly calibrated.

Step 1: Data collection

Given the process parameters specified in the design, a number of training samples are fabricated. The required sample size for training is determined by the process variability and measurement system capability. Subsequently, all the samples need to go through a postmanufacturing inspection process using the XCT machine. All the available training samples can be divided into two portions with 80% for model training and 20% for validation.

Step 2: Data preprocessing

Melt pool images need to be labeled with their corresponding coordinates in the final build based on the g-codes used during the fabrication. The porosity locations obtained from the XCT scanning should be matched with the derived melt pool locations to label the melt pool images as healthy or unhealthy. In addition, the corrupted images with no melt pool observed need to be removed from the thermal history.

Step 3: Data transformation

Each melt pool image should be cropped using the same cropping parameters to make sure all the melt pools can be included by the cropped images. Subsequently, spherical transformation and biharmonic surface interpolation are implemented to further reduce the dimension of the melt pool images.

Step 4: Model training

Step 4.1: MPCA. Using the training set, multilinear principal components analysis is applied to reduce the dimension and extract the relevant features as a low-dimensional tensor (core tensor). The entries in the core tensor are the extracted PCs used to construct the layer-wise features for quality prediction, and the projection matrices are obtained for future dimension reduction.

Step 4.2: Layer-wise feature extraction. The primary feature (volume of convex hull) should be calculated based on different possible numbers of PCs used, and the secondary feature (maximum norm of residuals) can also be calculated.

Step 5: Model selection

Using the validation set, the number of PCs with the best classification performance can be selected as the parameter to use for future in situ prediction. In addition, the corresponding SVM classifier using the selected optimal parameter can be obtained.

Step 6: In situ layer-wise prediction for new data

Step 6.1: For each newly fabricated part, the melt pool images of each layer can be collected during the build and analyzed by following the same procedure in Steps 2 and 3.

Step 6.2: MPCA-based dimension reduction can be achieved using the projection matrices estimated in Step 4.1.

Step 6.3: Based on the selected optimal number of PCs found in Step 5, the primary and secondary features can be calculated.

Step 6.4: Based on the extracted layer-wise features, the SVM classifier trained in Step 5 can be used for anomaly detection for each layer.

Acknowledgment

Research was sponsored by the Army Research Laboratory and was accomplished under Cooperative Agreement Number

Downloaded From: https://manufacturingscience.asmedigitalcollection.asme.org on 06/22/2019 Terms of Use: http://www.asme.org/about-asme/terms-of-use

W911NF-15-2-0025 (Funder ID: 10.13039/100006754). The views and conclusions contained in this document are those of the authors and should not be interpreted as representing the official policies, either expressed or implied, of the Army Research Laboratory or the U.S. Government. The U.S. Government is authorized to reproduce and distribute reprints for Government purposes notwithstanding any copyright notation herein.

References

[1] Grasso, M., and Colosimo, B. M., 2017, "Process Defects and In Situ Monitoring Methods in Metal Powder Bed Fusion: A Review," Meas. Sci. Technol., **28**(4), p. 044005.

[2] NIST, 2013, *Measurement Science Roadmap for Metal-Based Additive Manufacturing*, National Institute of Standards and Technology, U.S. Department of Commerce, Energetics Incorporated, Columbia, MD.

[3] America Makes, 2017, "Standardization Roadmap for Additive Manufacturing," ANSI.

[4] Matsumoto, M., Shiomi, M., Osakada, K., and Abe, F., 2002, "Finite Element Analysis of Single Layer Forming on Metallic Powder Bed in Rapid Prototyping by Selective Laser Processing," Int. J. Mach. Tools Manuf., **42**(1), pp. 61–67.

[5] Kolossov, S., Boillat, E., Glardon, R., Fischer, P., and Locher, M., 2004, "3D FE Simulation for Temperature Evolution in the Selective Laser Sintering Process," Int. J. Mach. Tools Manuf., **44**(2–3), pp. 117–123.

[6] Crespo, A., Deus, A. M., and Vilar, R., 2006, "Finite Element Analysis of Laser Powder Deposition of Titanium," Proceedings of ICALEO, Scottsdale, AZ, 2005, pp. 1016–1021.

[7] Martukanitz, R., Michaleris, P., Palmer, T., DebRoy, T., Liu, Z.-K., Otis, R., Heo, T. W., and Chen, L.-Q., 2014, "Toward an Integrated Computational System for Describing the Additive Manufacturing Process for Metallic Materials," Addit. Manuf., **1–4**, pp. 52–63.

[8] Hu, D., and Kovacevic, R., 2003, "Sensing, Modeling and Control for Laser-Based Additive Manufacturing," Int. J. Mach. Tools Manuf., **43**(1), pp. 51–60.

[9] Chen, T., and Zhang, Y., 2004, "Numerical Simulation of Two-Dimensional Melting and Resolidification of a Two-Component Metal Powder Layer in Selective Laser Sintering Process," Numer. Heat Trans. A Appl., **46**(7), pp. 633–649.

[10] Grasso, M., Laguzza, V., Semeraro, Q., and Colosimo, B. M., 2016, "In-Process Monitoring of Selective Laser Melting: Spatial Detection of Defects Via Image Data Analysis," ASME J. Manuf. Sci. Eng., **139**(5), p. 051001.

[11] Grasso, M., Demir, A. G., Previtali, B., and Colosimo, B. M., 2018, "In Situ Monitoring of Selective Laser Melting of Zinc Powder Via Infrared Imaging of the Process Plume," Robot. Comput. Integr. Manuf., **49**, pp. 229–239.

[12] Khanzadeh, M., Chowdhury, S., Tschopp, M. A., Doude, H. R., Marufuzzaman, M., and Bian, L., 2018, "In-Situ Monitoring of Melt Pool Images for Porosity Prediction in Directed Energy Deposition Processes," IISE Trans. **51**(5), pp. 1–19.

[13] Liu, J., Liu, C., Bai, Y., Rao, P., Williams, C., and Kong, Z., 2018, "Layer-Wise Spatial Modeling of Porosity in Additive Manufacturing," IISE Trans., **51**(2), pp. 109–123.

[14] Sharratt, B. M., 2015, "Non-Destructive Techniques and Technologies for Qualification of Additive Manufactured Parts and Processes," Defence Research Reports.

[15] Montazeri, M., Yavari, R., Rao, P., and Boulware, P., 2018, "In-Process Monitoring of Material Cross-Contamination Defects in Laser Powder Bed Fusion," ASME J. Manuf. Sci. Eng., **140**(11), p. 111001.

[16] Imani, F., Gaikwad, A., Montazeri, M., Rao, P., Yang, H., and Reutzel, E., 2018, "Process Mapping and In-Process Monitoring of Porosity in Laser Powder Bed Fusion Using Layerwise Optical Imaging," ASME J. Manuf. Sci. Eng., **140**(10), p. 101009.

[17] Montazeri, M., and Rao, P., 2018, "Sensor-Based Build Condition Monitoring in Laser Powder Bed Fusion Additive Manufacturing Process Using a Spectral Graph Theoretic Approach," ASME J. Manuf. Sci. Eng., **140**(9), p. 091002.

[18] Yao, B., Imani, F., Sakpal, A. S., Reutzel, E. W., and Yang, H., 2018, "Multifractal Analysis of Image Profiles for the Characterization and Detection of Defects in Additive Manufacturing," ASME J. Manuf. Sci. Eng., **140**(3), p. 031014.

[19] Plott, J., Tian, X., and Shih, A., 2018, "Measurement and Modeling of Forces in Extrusion-Based Additive Manufacturing of Flexible Silicone Elastomer With Thin Wall Structures," ASME J. Manuf. Sci. Eng., **140**(9), p. 091009.

[20] Corbin, D. J., Nassar, A. R., Reutzel, E. W., Beese, A. M., and Michaleris, P., 2018, "Effect of Substrate Thickness and Preheating on the Distortion of Laser Deposited Ti–6Al–4V," ASME J. Manuf. Sci. Eng., **140**(6), p. 061009.

[21] Khanzadeh, M., Rao, P., Jafari-Marandi, R., Smith, B. K., Tschopp, M. A., and Bian, L., 2017, "Quantifying Geometric Accuracy With Unsupervised Machine Learning: Using Self-Organizing Map on Fused Filament Fabrication Additive Manufacturing Parts," ASME J. Manuf. Sci. Eng., **140**(3), p. 031011.

[22] Samie Tootooni, M., Dsouza, A., Donovan, R., Rao, P. K., (James) Kong, Z., and Borgesen, P., 2017, "Classifying the Dimensional Variation in Additive Manufactured Parts From Laser-Scanned Three-Dimensional Point Cloud Data Using Machine Learning Approaches," ASME J. Manuf. Sci. Eng., **139**(9), p. 091005.

[23] Chowdhury, S., Mhapsekar, K., and Anand, S., 2017, "Part Build Orientation Optimization and Neural Network-Based Geometry Compensation for Additive Manufacturing Process," ASME J. Manuf. Sci. Eng., **140**(3), p. 031009.

[24] Brika, S. E., Zhao, Y. F., Brochu, M., and Mezzetta, J., 2017, "Multi-Objective Build Orientation Optimization for Powder Bed Fusion by Laser," ASME J. Manuf. Sci. Eng., **139**(11), p. 111011.

[25] Aboutaleb, A. M., Tschopp, M. A., Rao, P. K., and Bian, L., 2017, "Multi-Objective Accelerated Process Optimization of Part Geometric Accuracy in Additive Manufacturing," ASME J. Manuf. Sci. Eng., **139**(10), p. 101001.

[26] Yan, J., Battiato, I., and Fadel, G. M., 2017, "A Mathematical Model-Based Optimization Method for Direct Metal Deposition of Multimaterials," ASME J. Manuf. Sci. Eng., **139**(8), p. 081011.

[27] Garnier, V., Piwakowski, B., Abraham, O., Villain, G., Payan, C., and Chaix, J. F., 2013, "Acoustic Techniques for Concrete Evaluation: Improvements, Comparisons and Consistency," Construct. Build. Mater., **43**, pp. 598–613.

[28] Soltani, F., Goueygou, M., Lafhaj, Z., and Piwakowski, B., 2013, "Relationship Between Ultrasonic Rayleigh Wave Propagation and Capillary Porosity in Cement Paste With Variable Water Content," NDT E Int., **54**, pp. 75–83.

[29] Cai, X., Malcolm, A. A., Wong, B. S., and Fan, Z., 2015, "Measurement and Characterization of Porosity in Aluminium Selective Laser Melting Parts Using X-Ray CT," Virtual Phys. Prototyp., **10**(4), pp. 195–206.

[30] Gibson, I., Rosen, D., and Stucker, B., 2015, "Directed Energy Deposition Processes," *Additive Manufacturing Technologies*, I. Gibson, ed., Springer, New York, NY, pp. 245–268.

[31] Ngo, T. D., Kashani, A., Imbalzano, G., Nguyen, K. T. Q., and Hui, D., 2018, "Additive Manufacturing (3D Printing): A Review of Materials, Methods, Applications and Challenges," Compos. B: Eng., **143**, pp. 172–196.

[32] Thompson, S. M., Bian, L., Shamsaei, N., and Yadollahi, A., 2015, "An Overview of Direct Laser Deposition for Additive Manufacturing; Part I: Transport Phenomena, Modeling and Diagnostics," Addit. Manuf., **8**, pp. 36–62.

[33] Costa, L., Reti, T., Deus, A., and Vilar, R., 2002, "Simulation of Layer Overlap Tempering Kinetics in Steel Parts Deposited by Laser Cladding," Proceedings of International Conference on Metal Powder Deposition for Rapid Manufacturing, Princeton, NJ, April, MPIF, pp. 172–176.

[34] Costa, L., Vilar, R., Reti, T., and Deus, A. M., 2005, "Rapid Tooling by Laser Powder Deposition: Process Simulation Using Finite Element Analysis," Acta Mater., **53**(14), pp. 3987–3999.

[35] Antony, K., Arivazhagan, N., and Senthilkumaran, K., 2014, "Numerical and Experimental Investigations on Laser Melting of Stainless Steel 316L Metal Powders," J. Manuf. Process., **16**(3), pp. 345–355.

[36] Foroozmehr, A., Badrossamay, M., Foroozmehr, E., and Golabi, S., 2016, "Finite Element Simulation of Selective Laser Melting Process Considering Optical Penetration Depth of Laser in Powder Bed," Mater. Des., **89**, pp. 255–263.

[37] Andreotta, R., Ladani, L., and Brindley, W., 2017, "Finite Element Simulation of Laser Additive Melting and Solidification of Inconel 718 With Experimentally Tested Thermal Properties," Finite Elements Anal. Des., **135**, pp. 36–43.

[38] Denlinger, E. R., Jagdale, V., Srinivasan, G. V., El-Wardany, T., and Michaleris, P., 2016, "Thermal Modeling of Inconel 718 Processed With Powder Bed Fusion and Experimental Validation Using In Situ Measurements," Addit. Manuf., **11**, pp. 7–15.

[39] Riedlbauer, D., Scharowsky, T., Singer, R. F., Steinmann, P., Körner, C., and Mergheim, J., 2017, "Macroscopic Simulation and Experimental Measurement of Melt Pool Characteristics in Selective Electron Beam Melting of Ti-6Al-4V," Int. J. Adv. Manuf. Technol., **88**(5–8), pp. 1309–1317.

[40] Roy, S., Juha, M., Shephard, M. S., and Maniatty, A. M., 2018, "Heat Transfer Model and Finite Element Formulation for Simulation of Selective Laser Melting," Comput. Mech., **62**(3), pp. 273–284.

[41] Pitassi, D., Savoia, E., Fontanari, V., Molinari, A., Luchin, V., Zappini, G., and Benedetti, M., 2018, "Finite Element Thermal Analysis of Metal Parts Additively Manufactured Via Selective Laser Melting," *Finite Element Method—Simulation, Numerical Analysis and Solution Techniques*, P. Răzvan, ed., InTechOpen, Rijeka, Croatia, pp. 123–154.

[42] Huang, Y., Yang, L. J., Du, X. Z., and Yang, Y. P., 2016, "Finite Element Analysis of Thermal Behavior of Metal Powder During Selective Laser Melting," Int. J. Therm. Sci., **104**, pp. 146–157.

[43] Tapia, G., King, W., Johnson, L., Arroyave, R., Karaman, I., and Elwany, A., 2018, "Uncertainty Propagation Analysis of Computational Models in Laser Powder Bed Fusion Additive Manufacturing Using Polynomial Chaos Expansions," ASME J. Manuf. Sci. Eng., **140**(12), p. 121006.

[44] Cheng, B., Lane, B., Whiting, J., and Chou, K., 2018, "A Combined Experimental-Numerical Method to Evaluate Powder Thermal Properties in Laser Powder Bed Fusion," ASME J. Manuf. Sci. Eng., **140**(11), p. 111008.

[45] Vastola, G., Pei, Q. X., and Zhang, Y. W., 2018, "Predictive Model for Porosity in Powder-Bed Fusion Additive Manufacturing at High Beam Energy Regime," Addit. Manuf., **22**, pp. 817–822.

[46] Bruna-Rosso, C., Demir, A. G., and Previtali, B., 2018, "Selective Laser Melting Finite Element Modeling: Validation With High-Speed Imaging and Lack of Fusion Defects Prediction," Mater. Des., **156**, pp. 143–153.

[47] Soro, N., Brassart, L., Chen, Y., Veidt, M., Attar, H., and Dargusch, M. S., 2018, "Finite Element Analysis of Porous Commercially Pure Titanium for Biomedical Implant Application," Mater. Sci. Eng. A, **725**, pp. 43–50.

Downloaded From: https://manufacturingscience.asmedigitalcollection.asme.org on 06/22/2019 Terms of Use: http://www.asme.org/about-asme/terms-of-use

[48] Li, J., Wang, Q., and (Pan) Michaleris, P., 2018, "An Analytical Computation of Temperature Field Evolved in Directed Energy Deposition," ASME J. Manuf. Sci. Eng., **140**(10), p. 101004.
[49] Baykasoglu, C., Akyildiz, O., Candemir, D., Yang, Q., and To, A. C., 2018, "Predicting Microstructure Evolution During Directed Energy Deposition Additive Manufacturing of Ti-6Al-4V," ASME J. Manuf. Sci. Eng., **140**(5), p. 051003.
[50] Li, C., Liu, Z. Y., Fang, X. Y., and Guo, Y. B., 2018, "On the Simulation Scalability of Predicting Residual Stress and Distortion in Selective Laser Melting," ASME J. Manuf. Sci. Eng., **140**(4), p. 041013.
[51] Thijs, L., Verhaeghe, F., Craeghs, T., Van Humbeeck, J., and Kruth, J.-P., 2010, "A Study of the Microstructural Evolution During Selective Laser Melting of Ti–6Al–4V," Acta Mater., **58**(9), pp. 3303–3312.
[52] Clijsters, S., Craeghs, T., Buls, S., Kempen, K., and Kruth, J.-P., 2014, "In Situ Quality Control of the Selective Laser Melting Process Using a High-Speed, Real-Time Melt Pool Monitoring System," Int. J. Adv. Manuf. Technol., **75**(5–8), pp. 1089–1101.
[53] Song, L., and Mazumder, J., 2011, "Feedback Control of Melt Pool Temperature During Laser Cladding Process," IEEE Trans. Control Syst. Technol., **19**(6), pp. 1349–1356.
[54] Lane, B., Moylan, S., Whitenton, E. P., and Ma, L., 2016, "Thermographic Measurements of the Commercial Laser Powder Bed Fusion Process at NIST," Rapid Prototyp. J., **22**(5), pp. 778–787.
[55] Cunningham, R., Narra, S. P., Montgomery, C., Beuth, J., and Rollett, A. D., 2017, "Synchrotron-Based X-Ray Microtomography Characterization of the Effect of Processing Variables on Porosity Formation in Laser Power-Bed Additive Manufacturing of Ti-6Al-4V," JOM, **69**(3), pp. 479–484.
[56] Dilip, J. J. S., Zhang, S., Teng, C., Zeng, K., Robinson, C., Pal, D., and Stucker, B., 2017, "Influence of Processing Parameters on the Evolution of Melt Pool, Porosity, and Microstructures in Ti-6Al-4V Alloy Parts Fabricated by Selective Laser Melting," Prog. Addit. Manuf., **2**(3), pp. 157–167.
[57] Tang, M., Pistorius, P. C., and Beuth, J. L., 2017, "Prediction of Lack-of-Fusion Porosity for Powder Bed Fusion," Addit. Manuf., **14**, pp. 39–48.
[58] Khanzadeh, M., Chowdhury, S., Marufuzzaman, M., Tschopp, M. A., and Bian, L., 2018, "Porosity Prediction: Supervised-Learning of Thermal History for Direct Laser Deposition," J. Manuf. Syst., **47**, pp. 69–82.
[59] Khanzadehdaghalian, M., Bian, L., Shamsaei, N., and Thompson, S. M., 2016, "Porosity Detection of Laser Based Additive Manufacturing Using Melt Pool Morphology Clustering," Solid Freeform Fabrication 2016: Proceedings of the 26th Annual International, Austin, TX, pp. 1487–1494.
[60] Kanko, J. A., Sibley, A. P., and Fraser, J. M., 2016, "In Situ Morphology-Based Defect Detection of Selective Laser Melting Through Inline Coherent Imaging," J. Mater. Process. Technol., **231**, pp. 488–500.
[61] Krauss, H., Eschey, C., and Zaeh, M., 2012, "Thermography for Monitoring the Selective Laser Melting Process," Proceedings of the Solid Freeform Fabrication Symposium, Austin, TX, pp. 999–1014.
[62] Lu, H., Plataniotis, K. N., and Venetsanopoulos, A. N., 2008, "MPCA: Multilinear Principal Component Analysis of Tensor Objects," IEEE Trans. Neural Netw., **19**(1), pp. 18–39.
[63] Matoušek, J., 2002, *Lectures on Discrete Geometry*, Vol. 212, Springer, New York.
[64] Barber, C. B., Dobkin, D. P., and Huhdanpaa, H., 1996, "The Quickhull Algorithm for Convex Hulls," ACM Trans. Math. Softw., **22**(4), pp. 469–483.
[65] Nelson, L. S., 1986, "Control Chart for Multiple Stream Processes," J. Qual. Technol., **18**(4), pp. 255–256.
[66] Kotsiantis, S. B., 2007, "Supervised Machine Learning: A Review of Classification Techniques," Informatica, **31**, pp. 249–268.
[67] Burges, C. J. C., 1998, "A Tutorial on Support Vector Machines for Pattern Recognition," Data Mining Knowl. Discov., **2**(2), pp. 121–167.
[68] Marshall, G. J., Thompson, S. M., and Shamsaei, N., 2016, "Data Indicating Temperature Response of Ti–6Al–4V Thin-Walled Structure During Its Additive Manufacture Via Laser Engineered Net Shaping," Data Brief, **7**, pp. 697–703.
[69] Khanzadeh, M., Tian, W., Yadollahi, A., Doude, H. R., Tschopp, M. A., and Bian, L., 2018, "Dual Process Monitoring of Metal-Based Additive Manufacturing Using Tensor Decomposition of Thermal Image Streams," Addit. Manuf., **23**, pp. 443–456.
[70] Dubitzky, W., Granzow, M., and Berrar, D. P., 2007, *Fundamentals of Data Mining in Genomics and Proteomics*, Springer Science & Business Media, New York.

Downloaded From: https://manufacturingscience.asmedigitalcollection.asme.org on 06/22/2019 Terms of Use: http://www.asme.org/about-asme/terms-of-use